

Laser-induced Coulomb explosion of 1,4–diiodobenzene molecules: Studies of isolated molecules and molecules in helium nanodroplets

Lars Christiansen and Jens H. Nielsen*

Department of Physics and Astronomy, Aarhus University, 8000 Aarhus C, Denmark

Lauge Christensen, Benjamin Shepperson, and Dominik Pentlehner

Department of Chemistry, Aarhus University, 8000 Aarhus C, Denmark

Henrik Stapelfeldt†

*Department of Chemistry, Aarhus University, 8000 Aarhus C, Denmark and**Interdisciplinary Nanoscience Center (iNANO), Aarhus University, 8000 Aarhus C, Denmark*

(Received 22 December 2015; published 10 February 2016)

Coulomb explosion of 1,4–diiodobenzene molecules, isolated or embedded in helium nanodroplets, is induced by irradiation with an intense femtosecond laser pulse. The recoiling ion fragments are probed by time-of-flight measurements and two-dimensional velocity map imaging. Correlation analysis of the emission directions of I^+ ions recoiling from each end of the molecules reveals significant deviation from axial recoil, i.e., where the I^+ ions leave strictly along the I-I symmetry axis. For isolated molecules, the relative angular distribution of the I^+ ions is centered at 180° , corresponding to perfect axial recoil, but with a full width at half maximum of 30° . For molecules inside He droplets, the width of the distribution increases to 45° . These results provide a direct measure of the accuracy of Coulomb explosion as a probe of the spatial orientation of molecules, which is particularly relevant in connection with laser-induced molecular alignment and orientation. In addition, our studies show how it is possible to identify fragmentation pathways of the Coulomb explosion for the isolated 1,4–diiodobenzene molecules. Finally, for the 1,4–diiodobenzene molecules in He droplets, it is shown that the angular correlation between fragments from the Coulomb explosion is preserved after they have interacted with the He environment.

DOI: [10.1103/PhysRevA.93.023411](https://doi.org/10.1103/PhysRevA.93.023411)

I. INTRODUCTION

Molecular Coulomb explosion is the process by which several electrons are rapidly removed from a molecule, and the resulting multiply charged molecular cation breaks apart into ionic fragments due to their mutual electrostatic repulsion. Originally introduced in experiments on collisions between a fast beam of singly charged molecular ions and a thin foil [1], Coulomb explosion imaging is a technique aimed at determining molecular structure by recording the final momenta of the recoiling ionic fragments.

Other means to induce Coulomb explosion have proven efficient and useful, in particular intense ultrashort laser pulses in the near-infrared or visible region [2], synchrotron radiation [3,4], and, more recently, free-electron laser pulses in the (soft) x-ray regime [5–7]. The use of ultrashort laser pulses has several advantages, notably that the timing of the Coulomb explosion event can be varied relative to another event. This allows for the Coulomb explosion event to be used as a time-resolved structural probe of molecular dynamics. Laser-induced Coulomb explosion has been employed in a variety of studies to image either static or time-dependent structures of molecules, including the determination of the absolute configuration of chiral molecules [8], photodissociation [9],

photoisomerization [10,11], charge transfer [7], and torsion of axially chiral molecules [12].

In addition to providing information about the intramolecular structure, the recoil directions of the fragment ions from laser-based Coulomb explosion also provide a direct measure of how molecules are turned in space [13,14]. This has been exploited extensively over the past 10–15 years in a wealth of studies on alignment and orientation of molecules induced by moderately intense laser pulses or by the combination of laser pulses and static electric fields [15,16]. The accuracy to which the emission direction of the fragment ions reflects the spatial orientation of the molecules at the instant the ultrashort laser pulse arrives depends on how precisely the fragments recoil along the bonds that are broken—a condition similar to the axial recoil approximation long discussed in photodissociation experiments [17–19].

For diatomic molecules, the conservation of momentum implies that the two positively charged fragments recoil exactly along the internuclear axis. Thus, if the Coulomb explosion is prompt, i.e., no metastable multiply charged cations are produced and the molecules are not excited to extremely high rotational states as in super-rotors [20], then the axial recoil is essentially perfect and the fragment recoil vectors are an accurate determination of the internuclear axis at the time of the short laser pulse.

For polyatomic molecules, additional factors can cause deviation from axial recoil, including the distortion of the molecular geometry during the Coulomb explosion process due to vibrations (such as bending) and charge-asymmetric explosion channels. To our knowledge, the question of the

*Present address: Research Software Development Group, Research IT Services, University College London, Podium Building (1st Floor), Gower Street, London WC1E 6BT, United Kingdom.

†Corresponding author: henriks@chem.au.dk

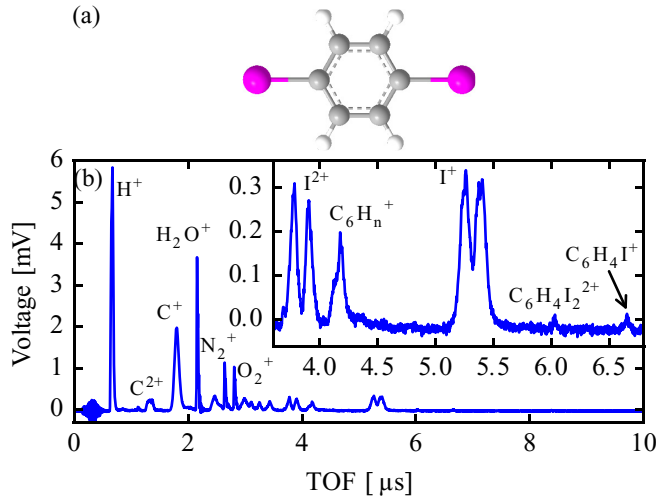


FIG. 1. (a) Sketch of the molecular structure of 1,4-diiodobenzene (DIB). (b) TOF mass spectrum of isolated DIB molecules recorded with the probe pulse polarized along the TOF axis. The intensity is 3.8×10^{14} W/cm². The predominant fragments are labeled. The inset shows a zoom of the region between 3.5 and 7 μ s covering fragments from $m/q = 57$ to $m/q = 210$ u/e.

accuracy of axial recoil in Coulomb explosion of polyatomic molecules has been only very sparsely addressed so far despite the rapidly growing interest for controlling alignment and orientation of complex molecules [12,21,22]. As such, we find it important to explore how precisely laser-induced Coulomb explosion imaging is capable of characterizing the spatial orientation of polyatomic molecules.

In the current work, we address this topic by quantitatively exploring the accuracy to which the principal symmetry axis of 1,4-diiodobenzene (DIB) molecules, i.e., the I-I axis [see Fig. 1(a)], can be determined through measurements of the recoil directions of the iodine ions. Being the most polarizable axis of the molecule, it is the I-I axis that will be aligned in one-dimensional (and three-dimensional) alignment schemes, both in the adiabatic and the nonadiabatic limit. Therefore, it is of interest to assess how well Coulomb explosion imaging measures the spatial orientation of the I-I axis. The studies are conducted both on isolated molecules and on molecules dissolved in helium nanodroplets—the latter situation being particularly important for new activities on laser-induced alignment of molecules embedded in He droplets [23–25].

II. EXPERIMENTAL SETUP

Most of the experimental setup has been described previously [23,24] and only a few details are given here. A sample of 1,4-diiodobenzene [structure shown in Fig. 1(a)] is placed inside a pulsed Even-Lavie valve [26], heated to 80 °C and coexpanded with 80 bar of helium. The resulting supersonic molecular beam passes through a 2 mm skimmer before entering the target region where it is crossed by a focused, pulsed, linearly polarized laser beam ($\lambda = 800$ nm, $\tau_{\text{FWHM}} = 30$ fs, $\omega_0 = 25$ μ m). The laser pulse is sufficiently intense to Coulomb explode DIB and the charged fragments produced by the explosion are guided onto a position-sensitive detector by

a velocity map imaging (VMI) spectrometer [27]. The detector allows for acquisition of time-of-flight (TOF) mass spectra or two-dimensional (2D) images of one or more ion species. The VMI voltages determine the arrival time of the ion species and the size of the 2D ion images. For measurements on isolated DIB molecules, the voltages were kept at $V_{\text{repeller}}/V_{\text{extractor}} = 3000$ V/2000 V, unless specifically mentioned otherwise. The He droplets used to solvate DIB molecules were produced by expanding ~ 25 bar of He gas, cryogenically precooled to 12 K through a 5 μ m orifice. These conditions produced He droplets consisting of $\sim 1.5 \times 10^4$ He atoms [28]. The droplet beam passes a pick-up cell where the partial pressure of DIB is adjusted to optimize for doping a single molecule into each droplet. The droplet beam then enters the target region and is crossed by the focused pulsed laser beam. For the measurements on DIB molecules in He droplets, the distance between the laser-molecule interaction point and the detector was increased by inserting a ~ 30 cm flight tube in order to enhance the temporal resolution of the TOF measurements. The increased flight distance requires the VMI voltage ratio to be modified to 8000 V/5025 V. For some of the TOF measurements on DIB in He droplets, a second focused pulsed laser beam was used to induce nonadiabatic alignment of the molecules prior to the Coulomb explosion. The Coulomb explosion pulse was sent at the time when the molecules were aligned the strongest—see Ref. [25] for details on the alignment dynamics.

III. COULOMB EXPLOSION OF ISOLATED DIB MOLECULES

Our measurements comprise (1) time-of-flight measurements to identify the different ion species created, and (2) two-dimensional images of different ion species, from which their radial and angular distributions are extracted. The latter enables correlations between the emission directions or velocities of different ions to be revealed through covariance analysis.

A. Time-of-flight measurements

Figure 1(b) shows the time-of-flight (TOF) spectrum when the DIB molecules are irradiated by the probe pulse with a peak intensity of 3.8×10^{14} W/cm², which is enough to multi-ionize the molecule and create many charged fragments. In the spectrum, the sharp features of H_2O^+ , N_2^+ , and O_2^+ all stem from the ionization of background gas in the target chamber. The spectrum is dominated by H^+ and C^+ ions, but the ions of interest are shown in the inset. Here the largest signals are identified as I^+ and I^{2+} , both of which have a distinct double-peak structure. The structure arises from the probe pulse being polarized along the TOF direction. The molecules are randomly oriented in space, but the molecules that per chance have their I-I axis pointing along the laser polarization are more easily multi-ionized due to enhanced ionization [29–31]. As a result, the I^+ (or I^{2+}) ions created with a velocity towards the detector form the early peak, and the I^+ (or I^{2+}) created with a velocity away from the detector form the late peak. The two-peak structure disappears when the polarization is turned perpendicular to the TOF direction.

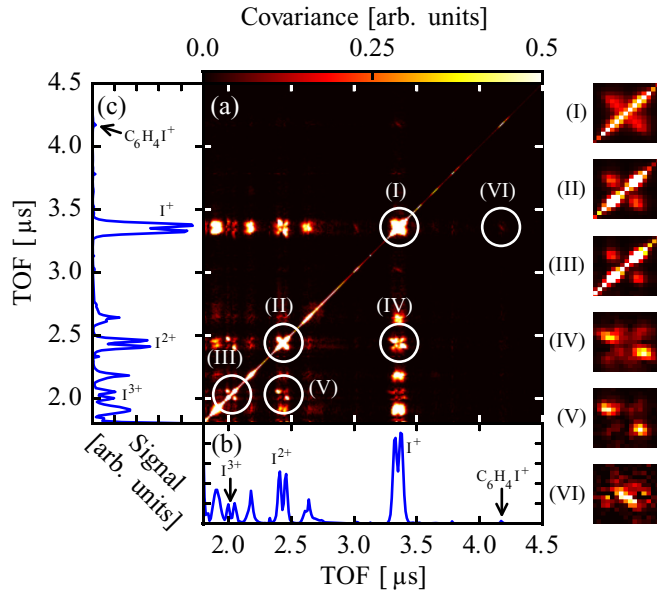


FIG. 2. (a) TOF covariance map for isolated DIB molecules. (b),(c) Average TOF spectrum. The panels (I–VI) show the covariance map for specific ion correlations with the color scale adjusted to enhance contrast. The insets are indicated on the main covariance maps by white circles.

Apart from the I^+ and I^{2+} fragments, the TOF spectrum consists mainly of remnants of a singly charged benzene ring ($C_6H_n^+$) and smaller hydrocarbon fragments. Near $6 \mu s$, the doubly charged parent ion is seen, $C_6H_4I_2^{2+}$. This proves the existence of states in the dication with lifetimes of at least microseconds [32]. Dications with a shorter lifetime would break apart before reaching the detector. At $6.7 \mu s$, a small amount of the $C_6H_4I^+$ fragment is detected. The singly charged parent ion is detected near $8.4 \mu s$ (not shown in the inset), but the signal is very weak. The DIB molecule appears to almost always fragment—even at lower intensities, very few unfragmented singly charged parent ions are observed.

To identify possible correlations between ion fragments, covariance mapping of the TOF signals was applied [33–36]. For these data, the extractor and repeller voltages were increased to 5333 and 8000 V, respectively, to enhance the detection efficiency and, at the same time, reduce the arrival time of all ionic species. The TOF spectrum for the i th laser shot represents the number of ions detected as a function of time x and is denoted $X_i(x)$. The time-of-flight covariance C is defined as

$$C(x, y) = \langle X_i(x)Y_i(y) \rangle - \langle X_i(x) \rangle \langle Y_i(y) \rangle, \quad (1)$$

where $\langle \cdot \rangle$ denotes the average over all laser shots. $C(x, y)$ is a measure for the correlation between ions recorded at time x with ions recorded at time y .

The covariance map obtained from the recording of 50 000 time-of-flight traces is shown in Fig. 2(a). Only the portion of the TOF spectrum corresponding to I^{3+} , I^{2+} , I^+ , $C_6H_4I_2^{2+}$, and $C_6H_4I^+$ is displayed. The covariance map is calculated according to Eq. (1), with X and Y being the same TOF spectrum; hence it is often referred to as an autovariance map. Below the covariance map [Fig. 2(b)] and to the left of it

[Fig. 2(c)], the average TOF spectrum is shown to ease the interpretation of the map.

The dominant signal along the diagonal from the lower-left to the upper-right corner is an artifact of the autovariance, since each ion will be correlated to itself. Away from the autovariance diagonal, hereafter termed the A diagonal, correlations between different ion species are observed. In particular, the correlations seen in the six areas, highlighted by white circles and numerated from (I) to (VI), are relevant. Closeups of these six areas are shown to the right of Fig. 2(a), with a color scale for each image providing the highest contrast. From (I), showing the correlation between I^+ ions, two regions symmetrically located on either side of the A diagonal indicate that some iodine ions arriving early on the detector are correlated to others arriving late. This is consistent with the polarization geometry of the probe pulse, predominantly ionizing along the flight direction, sending one I^+ towards the detector (arriving early) and one away from the detector (arriving late). Similar structures are seen for I^{2+} (II) and I^{3+} (III) ions, where a clear separation from the A diagonal is now apparent. This is because the higher charge states are primarily formed from ionization of the molecules that by chance are best aligned with the laser polarization, i.e., the forward-backward emission becomes very well defined.

Turning to (IV)–(VI), these show correlations between different ion species. Panel (IV) reveals correlations between I^+ and I^{2+} . The majority of the signal is confined to two areas symmetrically located on either side of the line parallel to the A diagonal, showing that some I^+ ions are created along with an I^{2+} partner from the same molecule. If the two ions were created from different molecules, it would be as likely to detect both ions arriving early or both arriving late, but no clear signal is observed parallel to the A diagonal. When created from the same molecule, the covariance signal must produce a pair of regions on either side of the A diagonal. The (small) signal observed parallel to the A diagonal cannot be due to emission of an (I^+, I^{2+}) ion pair from the same molecule because it would imply that either I^+ and I^{2+} both fly towards or both fly away from the detector. Instead, these false covariances are attributed to small fluctuations in target density which is known to generate false covariances, i.e., due to accidental covariance of an ion pair from different molecules [35,36]. Similar observations can be seen for (V) showing the correlation between I^{2+} and I^{3+} but with fewer false covariances, likely due to the lower count rate for these two species [35]. Panel (VI) shows the correlation between I^+ and $C_6H_4I^+$, which is very weak, but a feature crosswise to the A diagonal is seen, thus indicating a correlation between the two ion species.

In summary, the covariance analysis shows unambiguously that the Coulomb explosion of isolated DIB molecules leads to emission of correlated $(I^+, C_6H_4I^+)$, (I^+, I^{2+}) and (I^{2+}, I^{3+}) ion pairs. Whether the correlation between emitted (I^+, I^+) , (I^{2+}, I^{2+}) , and (I^{3+}, I^{3+}) ion pairs results from false covariances or true correlations cannot unambiguously be determined due to the intense autovariance signal. More extensive information of the Coulomb explosion of the molecules can be accessed by recording and analyzing 2D velocity ion images of the fragments, as discussed in the next section.

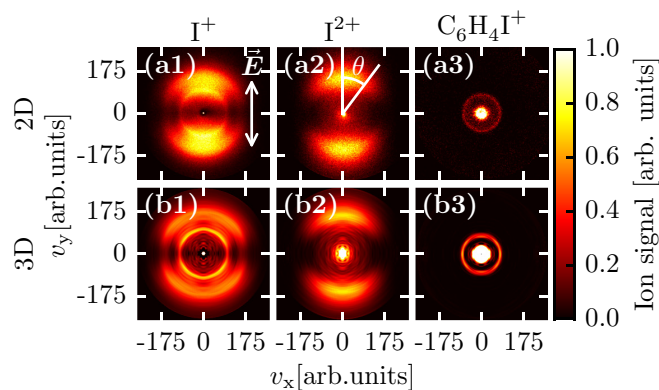


FIG. 3. (a1)–(a3) 2D ion images from isolated DIB molecules and (b1)–(b3) slices of the 3D ion distribution. Column (1): I^+ ions; column (2): I^{2+} ions; column (3): $C_6H_4I^+$ ions. The probe pulse polarization is indicated in (a1). Each image is scaled to its maximum value and is 551 by 551 pixels, which corresponds to 36 by 36 mm on the detector. See text for details.

B. Ion images

Two-dimensional velocity ion images are shown in the upper row of Fig. 3, where Fig. 3(a1) displays the distribution of I^+ ions. The probe pulse is polarized vertically, and a clear angular confinement of the ions along the polarization axis is observed. As discussed for the TOF spectra, this is a consequence of the orientational dependence of the ionization rate—with those molecules that happen to have their I-I axis pointing along the polarization being most efficiently ionized. Each image in the figure is scaled to the maximum value of a single pixel, and thus intensity across images cannot be compared. The peak intensity of the probe pulse was 4.8×10^{14} W/cm² for all images. The I^+ image contains two distinct pairs of half rings, indicating at least two fragmentation pathways leading to the generation of an I^+ ion. The signal near the center is ascribed to I^+ ions formed by single ionization of the molecules and subsequent dissociation of the cation into an I^+ ion and a neutral partner. These ions detected in the center constitute about 2% of the total amount of ions.

Due to the cylindrical symmetry of the experiment, the full three-dimensional (3D) velocity distribution can be obtained by an Abel inversion algorithm. Here the pBASEX software [37] was used to produce a slice of the 3D velocity distribution, which is shown in Figs. 3(b1)–3(b3). In the 3D image of I^+ ions [Fig. 3(b1)], the two half rings appear sharper. In the following, these two rings will be referred to as the inner and outer channel. For the I^{2+} ion image [Fig. 3(a2)], the emission direction is also confined along the laser polarization direction and only a single channel is visible. Performing the Abel inversion does not reveal more structure in the ion image [Fig. 3(b2)]. In addition, the VMI voltages were increased to search for additional higher-energy channels, producing I^{2+} ions, but none were observable within the limits of the setup.

The ion image of $C_6H_4I^+$ [Fig. 3(a3)] lacks the anisotropy seen for I^+ and I^{2+} . The majority of the signal is detected near the center, but a ring is visible at a slightly larger radius. The $C_6H_4I^+$ ions detected in the outermost ring must have

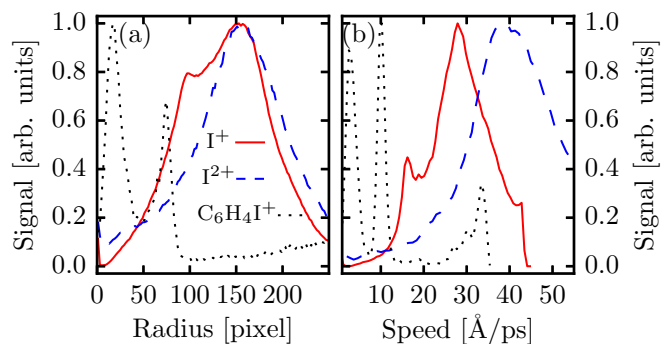


FIG. 4. (a) Radial distributions and (b) speed distributions of I^+ ions (solid red), I^{2+} ions (dashed blue), and $C_6H_4I^+$ ions (dotted black) obtained from the ion images in Figs. 3(a1)–3(a3) and 3(b1)–3(b3), respectively.

obtained their kinetic energy through repulsion with another charged fragment, which has to be an iodine ion. We believe that the lack of anisotropy results from the precursor dication, $C_6H_4I^{2+}$, living long enough that it can rotate a few or several times before it breaks up into a $C_6H_4I^+$ ion and an I^+ ion. The rotation time of DIB is ~ 3.17 nanoseconds, so the lifetime of the dication should be on the order of nanoseconds or tens of nanoseconds. Such lifetimes have been observed for dications of other molecules—for instance, CO_2 [38].

The fastest $C_6H_4I^+$ ions are emitted with a very distinct absolute velocity, suggesting that only a single fragmentation pathway is leading to this fragment. The signal near the center is likely from a breakup of the singly charged parent ion, similar to what was observed in the I^+ image. The Abel inverted image [Fig. 3(b3)] is not very different from the 2D ion image, but since the number of $C_6H_4I^+$ ions detected is only about 5% of the number of I^+ ions detected, the inversion algorithm introduces a lot of noise.

From the 2D ion images, the radial distribution is obtained by an angular integration. In Fig. 4(a), the radial distributions are shown for I^+ ions (solid red), I^{2+} ions (dashed blue), and $C_6H_4I^+$ ions (dotted black), with the x axis represented in pixels of the CCD camera. All distributions have been scaled to their maximum value to ease comparison. The two channels from the I^+ ion image are visible in the distribution at about 100 pixels for the inner and at 155 pixels for the outer. The I^{2+} signal peaks at a radius of about 155 pixels and has a very broad distribution, whereas the $C_6H_4I^+$ distribution is sharply peaked at 75 pixels. The signal in the $C_6H_4I^+$ distribution below 20 pixels is due to the ions detected near the center.

The radial distributions obtained from the 3D ion images can be converted to a speed distribution by calibrating the VMI spectrometer. Here the calibration was done by performing above threshold ionization (ATI) on argon and detecting discrete photoelectron energies separated by one photon energy in a 3D inverted image [39]. In Fig. 4(b), the speed distributions for the three different ion species are shown. Each distribution is scaled to the maximum value. From the speed distributions, the kinetic-energy distributions are obtained. The result for the I^+ ions is displayed in Fig. 5. It shows the two distinct peaks pertaining to the two Coulomb explosion channels. In particular, the outermost channel is observed to

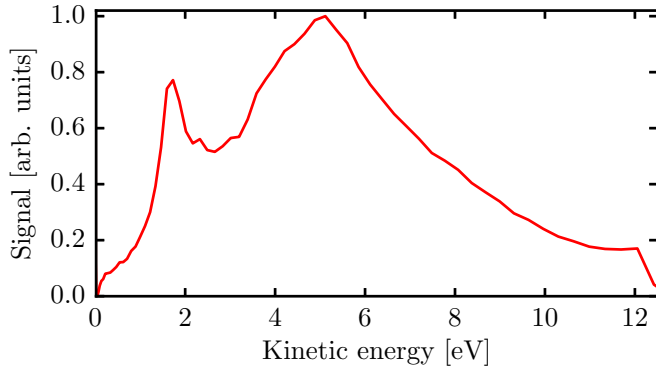


FIG. 5. The kinetic-energy distribution of I^+ ions resulting from ionization of the DIB molecules with a probe pulse intensity of 4.1×10^{14} W/cm².

peak at 5.1 eV—information that we will use below to identify the details of the Coulomb fragmentation.

C. Covariance analysis of the radial and angular distributions of the I^+ ions

The image of I^+ ions in Fig. 3(a1) consists of 2.5×10^6 ion hits recorded in 10^5 laser shots. With the coordinates for each ion hit saved along with the image number in which the laser shot was recorded, the covariance between different observables can be calculated. Whether ions recorded in either channel are correlated to other I^+ ions can be investigated by a radial covariance map. Now the observables X_i and Y_i in Eq. (1) are the radial distribution on the bottom half and the top half of the images, respectively, for the i th laser shot. The covariance map is shown in Fig. 6(a) along with the average radial distribution below [Fig. 6(b)] and to the left [Fig. 6(c)]

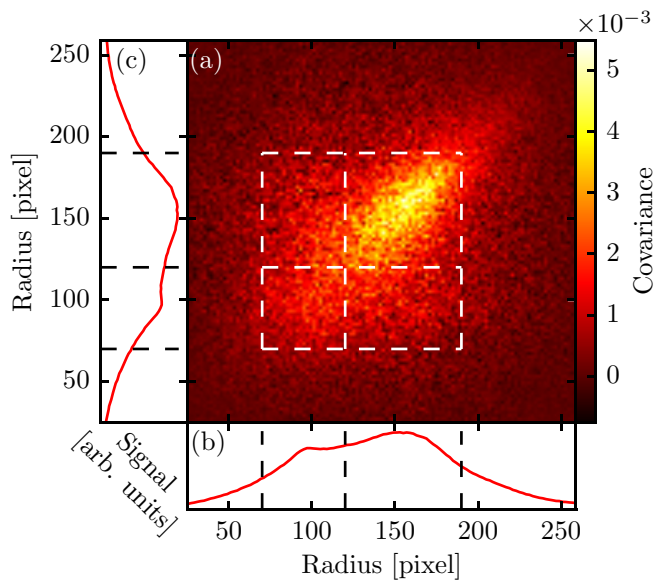


FIG. 6. (a) Radial covariance map of I^+ ions on the top half of the detector with the I^+ ions on the bottom half. (b),(c) Average radial distribution from 2D ion images. The dashed lines are guides to help distinguish regions for the two separate channels.

to ease interpretation. The radial distribution is the same as the one shown in Fig. 4(a).

In the radial distributions, three dashed lines have been drawn to separate the inner and outer channel. The intersection of the dashed lines creates four areas in the covariance map. The majority of the covariance signal is found in the top right area, which shows correlations between two I^+ ions in the outer channel. When detecting an I^+ ion in the outer channel on the top part of the detector, it is likely to detect another I^+ ion in the outer channel on the bottom half. In the top-left and bottom-right areas, there is almost no covariance signal, indicating no correlation between ions detected in different channels. The only way to create two I^+ ions with different velocities would be to remove a third electron closer to one iodine than the other. This seems unlikely in a molecule as symmetric as DIB. In the area containing only the inner channel, very little correlation signal is present. This implies that formation of an I^+ ion in the inner channel together with another I^+ ion is unlikely, thus instead some other charged fragment is produced. The small signal is believed to be due to the projection of ions stemming from the outer channel.

The covariance map shows that some of the I^+ ions detected in the outer channel are created with another I^+ ion in the outer channel. Such an I^+ ion pair could, in principle, originate from doubly ionized DIB molecules breaking up into two I^+ ions and a neutral C_6H_4 ring. With an equilibrium I-I distance of 6.82 Å [40], each I^+ ion would acquire a kinetic energy of 1.06 eV, from the electrostatic repulsion, which is significantly below that observed for the outer channel—see Fig. 5. Thus, a third electron must be removed from the molecule to release more energy in the Coulomb explosion process. If this extra ionization is assumed to create a single positive charge in the center of the aromatic ring, the kinetic energy of the I^+ ions detected would be 5.28 eV, which fits very well with the observed kinetic-energy distribution.

As such the combined information from the radial covariance map in Fig. 6 and the kinetic-energy distribution points to that the fragmentation pathway $C_6H_4I_2^{3+} \rightarrow I^+ + C_6H_4^+ + I^+$ makes a major contribution to the outermost channel observed in the I^+ image. Our analysis, however, shows that other fragmentation pathways are likely to contribute to the outer I^+ channel in order to account for the larger kinetic energies extending out to 10 eV. The assignment of the inner channel will be discussed in the next section.

The radial covariance map only describes the energetics of the correlated I^+ ions, but nothing about their mutual emission direction. If the angular emission direction of the ions is used as an observable, the covariance map is termed an angular covariance map [12,41,42]. The angular covariance map for I^+ ions is shown in Fig. 7 for the inner channel [Fig. 7(a)] and the outer channel [Fig. 7(b)]. Here, θ_1 and θ_2 are measures of the angle between the probe pulse polarization (vertical) and the vector for the ion hit, as defined in Fig. 3(a2). The covariance map is an autocovariance map since θ_1 and θ_2 refer to the same angle and, in order to avoid the large A-diagonal signal, the center line has been put to zero. Since only a weak covariance signal was observed for the inner channel in the radial covariance map, it is to no surprise that the angular covariance signal of the inner channel is about a factor of 4 weaker than the outer channel. The correlations in the inner

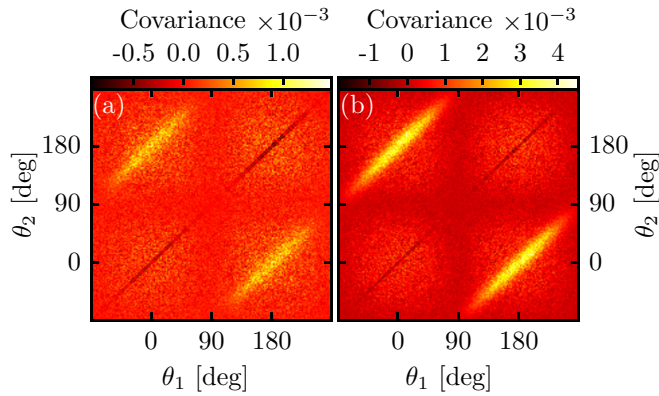


FIG. 7. Angular covariance map for I^+ ions detected in (a) the inner channel and (b) the outer channel as a function of emission angle θ_1 and θ_2 . The A-diagonal line has been put to zero.

channel are believed to stem from the tail of the outer channel, and hence the following discussion will focus on the outer channel.

In the covariance map displayed in Fig. 7(b), two oblong islands with prominent correlation are observed. The islands are centered along lines given by $\theta_2 = \theta_1 + 180^\circ$ and $\theta_2 = \theta_1 - 180^\circ$, which implies that the two I^+ ions are emitted with a relative angle of approximately 180° . This is in line with our expectations based on the assignment of the Coulomb fragmentation pathway responsible for the outer I^+ channel. A more straightforward view of the relative emission is obtained when the covariance map is rotated to show the difference angle $\theta_2 - \theta_1$ on one of the axes—see Fig. 8(a). The covariance signal is peaked around $\theta_1 = 0^\circ$ and $\theta_1 = 180^\circ$ due to the orientational selectivity of the ionization process: molecules with their I-I axis aligned along the probe polarization experience the highest ionization rate.

A particularly interesting feature of the observed islands is their width along the difference angle $\theta_2 - \theta_1$. Had the two I^+ ions recoiled exactly along the I-I axis of the molecule, which is the same direction as the bond each iodine atom makes to the central aromatic ring, the islands should have been narrow

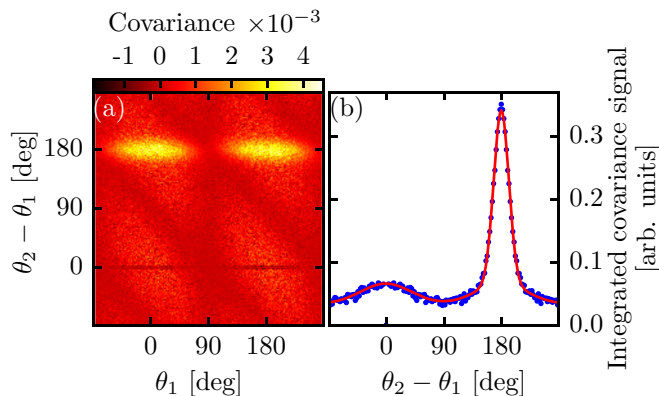


FIG. 8. (a) Angular covariance map for I^+ ions detected in the outer channel as a function of emission angle θ_1 and difference angle $\theta_2 - \theta_1$. (b) Integrated covariance as a function of the difference angle $\theta_2 - \theta_1$; see text for details.

lines. This is not the case and the finite width provides a direct measure of the deviation from axial recoil.

To obtain a quantitative measure for the deviation from axial recoil, the covariance map is integrated along the angle θ_1 . This gives the distribution shown by the blue dots in Fig. 8(b). It is peaked around 180° with a broader and weaker feature near 0° . The broad distribution around 0° must be false covariances, since it is not possible for both I^+ ions from the same molecule to be emitted in the same direction. Two I^+ ions can only be detected in the same direction if they come from two different molecules. It must be equally likely that the two I^+ ions created from two different molecules fly in opposite directions as it is likely that they fly in the same direction. Thus the false covariances must also be present around 180° . The red curve in Fig. 8(b) is the fit obtained by using three Gaussian shapes. First the false covariances near 0° are fitted to a Gaussian function. This shape is forced onto the distribution near 180° and the remaining data is fitted to a third Gaussian shape. From the fit, a full width at half maximum (FWHM) value of $28 \pm 0.2^\circ$ is extracted for the true covariance signal. This width gives a measure for the deviation from axial recoil. Further discussion of axial recoil is given below.

D. Covariance analysis of different ion species

To identify possible correlations between different ion species, images of the different ion species must be compiled at the same time. Ideally this is done by recording each ion species individually for each laser shot as is possible, for instance, by using a PImMS camera because it places a time stamp when each ion is detected instead of using a selective gate [42–44]. Here, we show that a regular CCD camera can also be used to identify correlations between selected different ion species simply by extending the gate window to encompass the pertinent ion species. In an effort to better understand what constitutes the inner channel in the I^+ image [Fig. 3(a1)], the detector gate window was extended (to span from 5.07 to 6.77 μs ; see Fig. 1) to simultaneously detect I^+ and $C_6H_4I^+$ ions, since fragmentation into these two fragments seemed like a plausible pathway. Although the different ions both are detected as a flash of light and thus cannot be distinguished on the detector, a covariance analysis provides new information. With the increased gate window, $C_6H_4I_2^{2+}$ ions will also be included in the detection, but since they all arrive at the center they should not influence the analysis.

To increase the probability of forming I^+ in the inner channel versus in the outer channel, the laser intensity was reduced to $2.1 \times 10^{14} \text{ W/cm}^2$. A total of 1.3×10^6 ions were detected in 2.4×10^5 laser shots, and from this a radial and an angular covariance analysis were performed. The radial covariance map is shown in Fig. 9(a) along with the average radial distribution in Figs. 9(b) and 9(c).

Extending the opening time of the detector can only lead to additional correlations compared to when only I^+ ions are imaged, and thus one should expect the same features as seen in Fig. 6. The average radial distributions have more ions shifted towards lower radii, which is a result of the lower laser intensity. Turning to the covariance map, the signal from the correlation between I^+ ions detected in the outer channel is still the most dominant one. The main difference to the covariance

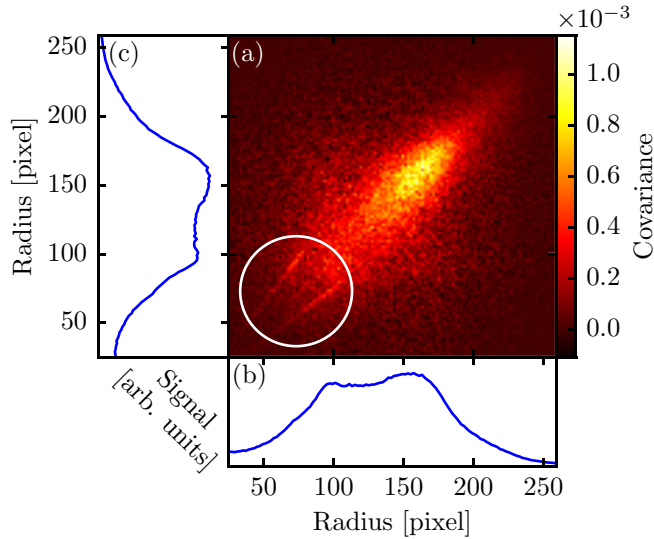


FIG. 9. (a) Radial covariance map for I^+ and $C_6H_4I^+$ ions on the top half of the detector with those on the bottom half. (b),(c) Average radial distribution including both ion species. The white circle highlights the main difference compared to Fig. 6.

map of only I^+ ions is the two sharp lines highlighted by the white circle. The sharp lines mean that when a given velocity of one of the ions is detected, the velocity of the other ion is fixed. This is characteristic of a two-body breakup where only two fragments can take away the energy and momentum. Since the sharp lines were not present in the radial covariance map of I^+ ions alone, it must be from the formation of an I^+ with a $C_6H_4I^+$ ion.

From momentum conservation, the speed of the I^+ ion will be M'/m' times the speed of the $C_6H_4I^+$ ion, where M' is the mass of C_6H_4I and m' is the mass of I . The radius reached on the detector by a fragment, R , is proportional to $v_{2D}TOF$, with v_{2D} being the magnitude of the velocity component in the detector plane. Since the TOF is proportional to $\sqrt{m/q}$, R can be expressed as $R \propto v_{2D}\sqrt{m}$. The ratio of the radius reached by the two fragments can now be calculated as

$$\frac{R_{I^+}}{R_{C_6H_4I^+}} \propto \sqrt{\frac{M'}{m'}}. \quad (2)$$

The mass of an I^+ ion and a $C_6H_4I^+$ ion is 127 and 203 u, respectively, and thus the slope of the line should be 1.26 or $\frac{1}{1.26}$ depending on which fragment is detected where. The measured slope of the lines was determined to be 1.30 and $\frac{1}{1.30}$. The good agreement between the measured and predicted slope shows that one possible outcome of Coulomb explosion of DIB molecules, pertaining to the inner I^+ channel, is the formation of an I^+ along with a $C_6H_4I^+$ partner.

Similarly to the I^+ ions alone, an angular covariance map was calculated with the long detector gate. Figure 10 shows the angular covariance map for the radial range covering the inner channel [Fig. 10(a)] and for the radial range covering the outer channel [Fig. 10(b)]. The outer channel appears the same as in Fig. 7, but the inner channel has a very sharp line given by $\theta_2 = \theta_1 + 180^\circ$ and $\theta_2 = \theta_1 - 180^\circ$, as indicated by

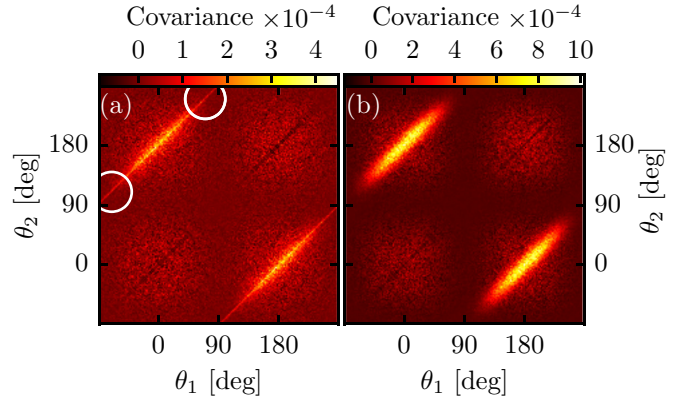


FIG. 10. Angular covariance map for a radial range covering (a) the inner channel and (b) the outer channel for I^+ ions. The white circle highlights the difference compared to Fig. 7.

the white circles. The width of the sharp line was determined to be $1.3 \pm 0.4^\circ$, which we assign to the resolution of the setup.

The sharp line extends across all angles of θ_1 but it is most clearly seen away from the correlations between two I^+ ions. This implies that the I^+ ions correlated to $C_6H_4I^+$ ions are emitted in all directions. This matches with the image of $C_6H_4I^+$ ions seen in Fig. 3(a3), where a uniform emission direction was observed. Likewise, a faint ring is observed for the I^+ ions in Fig. 3(a1) near the inner channel. This result proves that the $I^+-C_6H_4I^+$ fragmentation channel originates from a precursor dication which lives, and thus rotates, at least a few nanoseconds such that the two fragment ions are emitted isotropically.

IV. COULOMB EXPLOSION OF DIB MOLECULES INSIDE HELIUM DROPLETS

This section details the studies of Coulomb explosion of DIB molecules inside helium droplets. This section is structured similarly to the previous section, but with more emphasis on the unique droplet effects. By comparing the results of isolated molecules to those of molecules inside helium droplets, the effect of the helium droplet can be probed.

A. Time-of-flight mass spectra

A TOF mass spectrum of the ionic species created following Coulomb explosion of DIB molecules inside helium droplets was recorded and shown in Fig. 11. The low density of doped He droplets results in a more noisy TOF spectrum compared to that obtained for the isolated molecules [Fig. 1(b)].

The largest signal in the TOF is from H_2O^+ ions due to water vapor in the target chamber. Other ions from the background gas in the target chamber are H^+ , H_2^+ , N_2^+ , O_2^+ , and CO_2^+ . Large signals are seen for small helium clusters, namely He^+ , He_2^+ , and He_3^+ (some of this peak stems from C^+), but clusters of up to He_{18}^+ have been observed. All helium clusters disappear for pure helium droplets with no dopants. A zoom of the high-mass region is shown in the inset, with the most dominant signal coming from I^+ ions near $6.5 \mu s$. The arrival time of an I^+ ion coming from a molecule inside a He droplet is different from that of an isolated molecule (Fig. 1)

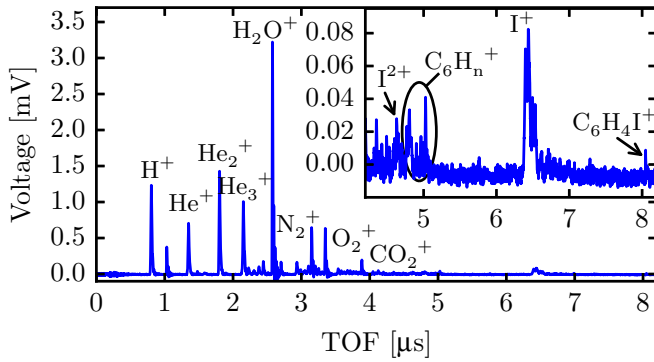


FIG. 11. TOF spectrum of DIB molecules inside helium droplets. The inset shows a zoom of the region between 4 and 8.2 μs covering fragments from $m/q = 46$ to $m/q = 210$ u/e. The main fragments are labeled. The probe pulse intensity was 4.5×10^{14} W/cm 2 and the polarization was along the TOF direction.

because of the addition of the flight tube. On the right side of the I^+ peak, a shoulder is visible, and some minor signals can be seen. The structure of these signals is discussed later in this section.

A high-statistics TOF spectrum was recorded focusing on the region of I^+ ions and higher masses—see Fig. 12(c). The time axis of the TOF spectrum has been converted to a mass scale to ease the interpretation. The largest signal is from I^+ ions and the splitting is caused by the polarization of the laser pulse as was the case for the isolated molecules. Every four mass units, a smaller replica of the main iodine signal is detected. This is interpreted as a IHe_n^+ complex. A similar structure in the TOF mass spectrum was observed for neutral I atoms formed via dissociation of molecules inside helium droplets [45].

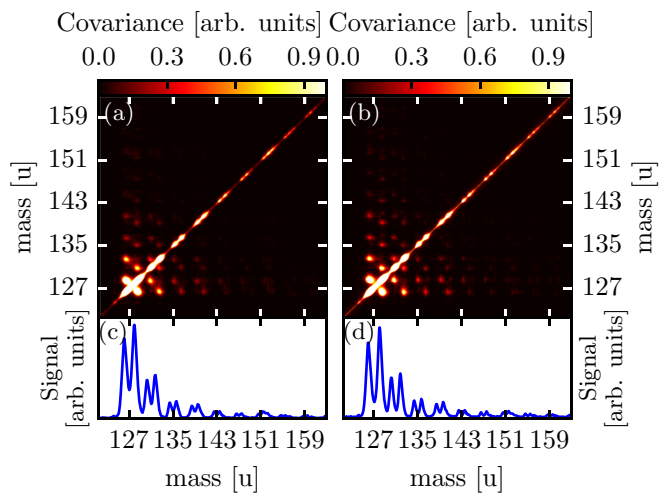


FIG. 12. (a) Time-of-flight covariance map for randomly aligned DIB molecules in helium droplets with the average TOF spectrum shown below in (c). (b) Time-of-flight covariance map for aligned DIB molecules in helium droplets with the average TOF spectrum shown below in (d). The intensity of the probe pulse was 2.2×10^{14} W/cm 2 and the polarization was along the TOF axis.

To investigate possible correlations between the fragment ions, the TOF covariance map, shown in Fig. 12(a), was calculated for 2.5×10^5 laser shots. The covariance map is dominated by the large autovariance signal along the central A diagonal, but signals away from the A diagonal can be seen as well. The strongest off-diagonal signal is the two lobes around (127,127), which indicate that forward I^+ ions are correlated to backward I^+ ions—just as in the isolated molecule case. In addition, a number of pairs of signals, completely absent for isolated molecules, are observed. These pairs consisting of two distinct regions along the direction approximately perpendicular to the A diagonal show pronounced correlations between forward and backward ions. For instance, the pairs around (127,131), (127,135), and (127,139) show unambiguously that forward (backward) I^+ ions are correlated to backward (forward) IHe^+ , IHe_2^+ , and IHe_3^+ ions. Likewise, the pairs around (131,135) and (131,139) show unambiguously that forward (backward) IHe^+ ions are correlated to backward (forward) IHe_2^+ and IHe_3^+ ions. The (131,131) pair indicates a correlation between forward and backward IHe^+ ions. Since the IHe_n^+ signal decreases as n increases, so does the correlation signals with IHe_n^+ ions.

To possibly reveal more correlations, alignment of the DIB molecules was induced by a 200-fs-long pulse pulse with a peak intensity of 1.6×10^{13} W/cm 2 . The probe pulse was sent 40 ps after the alignment pulse—just at the time where the degree of alignment reaches its highest value [23,25]. The molecules were aligned in the same direction as the probe pulse polarization, i.e., along the flight direction. The TOF covariance map for the aligned molecules is shown in Fig. 12(b) and the average TOF spectrum is shown in Fig. 12(d).

The alignment results in two obvious changes. First, the splitting of the I^+ and IHe_n^+ TOF signals in a forward and a backward peak is more pronounced. It is caused by the fact that more molecules are now aligned along the TOF direction, which adds signal to the peaks, and less molecules are perpendicular to the TOF axis, which increases the dip between the peaks. Second, all covariance signals appear stronger and the distance between the two areas in each covariance region increases. The explanation is the same as for the more pronounced splitting of the TOF peaks. The increased contrast of the covariance map implies that correlations between I^+ and IHe_5^+ are just visible.

Overall, the TOF covariance analysis shows that the pronounced correlation between a forward and a backward I^+ ion is preserved when either one or both of the I^+ ions interact with the He environment and a complex is formed with a number of helium atoms. In the next section, 2D velocity ion images will be used to learn more about the I^+ and IHe^+ ions produced by Coulomb explosion of DIB molecules inside helium droplets.

B. Ion images

As can be seen from the TOF mass spectrum in Fig. 11, the signal corresponding to I^{2+} and $\text{C}_6\text{H}_4\text{I}^+$ is quite weak and, in addition, the I^{2+} signal is overlapped with contributions from the He_n^+ progression. Therefore, we focus on the I^+ and IHe^+ ions. Figures 13(a1)–13(a3) show 2D velocity ion images recorded following Coulomb explosion of DIB

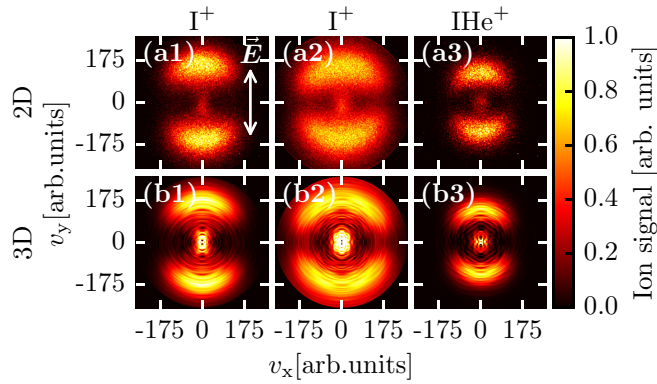


FIG. 13. (a1)–(a3) 2D ion images from DIB molecules in helium droplets and (b1)–(b3) slices of the 3D ion distribution. Column (1): I^+ ions recorded at a peak pulse intensity of 1.9×10^{14} W/cm 2 ; column (2): I^+ ions recorded at peak intensity of 3.8×10^{14} W/cm 2 ; column (3): IHe^+ ions recorded at a peak intensity of 1.9×10^{14} W/cm 2 . The laser polarization is indicated in (a1). Each image is 551 pixels by 551 pixels, which corresponds to 36 mm by 36 mm on the detector.

molecules inside helium droplets. I^+ ion images are shown in Figs. 13(a1) and 13(a2) recorded with an intensity of 1.9×10^{14} and 3.8×10^{14} W/cm 2 , respectively. The image in Fig. 13(a3) shows IHe^+ ions recorded for the low intensity.

The I^+ ion images show no sign of distinct fragmentation channels, in contrast to the situation for the isolated DIB molecules (Fig. 3). This is in line with what was observed for other molecules [23,24] and ascribed to the exchange of momentum and energy between the fragments and the surrounding He atoms during the Coulomb explosion. Each ion image is scaled to its maximum value on a single pixel, and thus comparison of count rates across the ion images is not possible. In Figs. 13(b1)–13(b3), a slice of the 3D ion distribution of the corresponding ions is shown. The 3D ion images do not immediately provide more information, but they allow for determination of the speed distributions.

Figure 14(a) displays the radial distributions from the 2D ion images for the I^+ ions recorded with high intensity

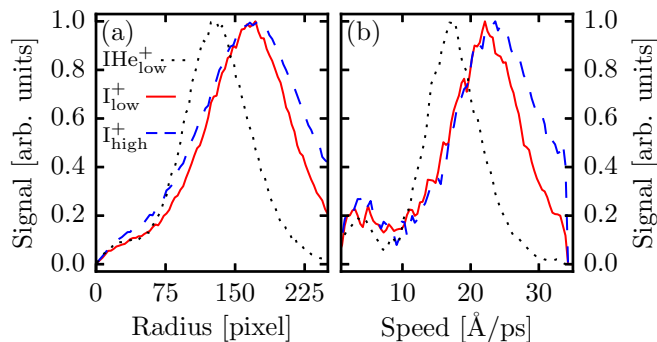


FIG. 14. (a) Radial distributions and (b) speed distributions of ions obtained from the images in Figs. 13(a1)–13(a3) and 13(b1)–13(b3), respectively. The distribution for I^+ ions recorded at an intensity of $I = 3.8 \times 10^{14}$ W/cm 2 is shown in dashed blue. The distributions for I^+ and IHe^+ ions at an intensity of $I = 1.9 \times 10^{14}$ W/cm 2 is shown in solid red and dotted black, respectively.

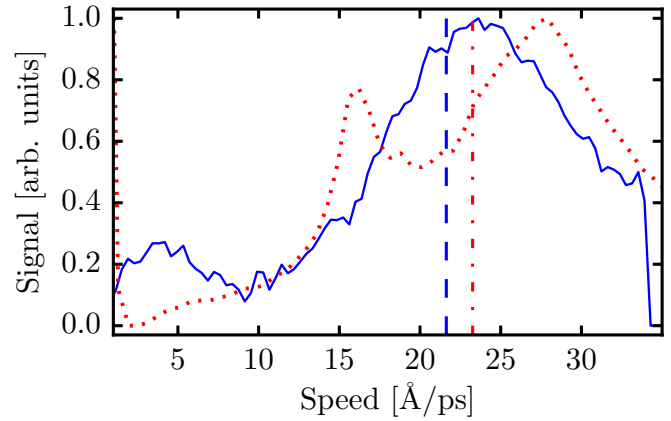


FIG. 15. Speed distribution of I^+ ions from isolated molecules for an intensity of 4.8×10^{14} W/cm 2 (dotted red) and for molecules in helium droplets for an intensity of 3.8×10^{14} W/cm 2 (solid blue). The dashed and dotted dashed line is the average speed for each distribution. See text for details.

(dashed blue) and low intensity (solid red), and for IHe^+ ions (dotted black). Comparing the red and blue curves, only minor differences are seen and, in both curves, only one channel is visible. The IHe^+ ions are detected at lower radii compared to the I^+ ions and the distribution is more sharply peaked. The speed distribution is obtained in the same manner as for the isolated molecules.

The speed distributions obtained from the 3D ion images are shown in Fig. 14(b). The sharp drop of the red and the blue curve at large speeds results from reaching the detector edge. The speed distribution for the high pulse intensity produces more I^+ ions at high speed, suggesting that the distribution consists of multiple components, some with different ionization states. The distribution of IHe^+ ions peaks about 5 Å/ps below the peak of the distribution for I^+ ions for the same intensity. Similar results were reported for photodissociation experiments [45,46]. The mass of the IHe^+ ion compared to the I^+ ion alone does not account for the discrepancy in velocity. However, IHe^+ may favorably be formed when other fragments also carry He atoms, increasing their masses also. Another possible explanation is that the IHe^+ ion is formed when the I^+ ion moves out of the droplet and that the probability of picking up a He atom is highest for slow I^+ ions.

The speed distributions of I^+ ions from isolated DIB molecules (dotted red) and from DIB molecules inside helium droplets (solid blue) are shown in Fig. 15. The dashed and dotted dashed line represent the average speed of the distribution. The I^+ ions are, on average, 7% faster from isolated molecules than from molecules inside helium droplets. The pulse intensity used for the isolated molecules was 4.8×10^{14} W/cm 2 , which is somewhat higher than the one used for molecules in droplets, 3.8×10^{14} W/cm 2 . However, even the average I^+ speed from Coulomb explosion of isolated molecules with a pulse intensity of 2.1×10^{14} W/cm 2 is higher than the average one from molecules inside droplets at an intensity of 3.8×10^{14} W/cm 2 . The average speed was calculated for ions detected between 2 and 34 Å/ps for both

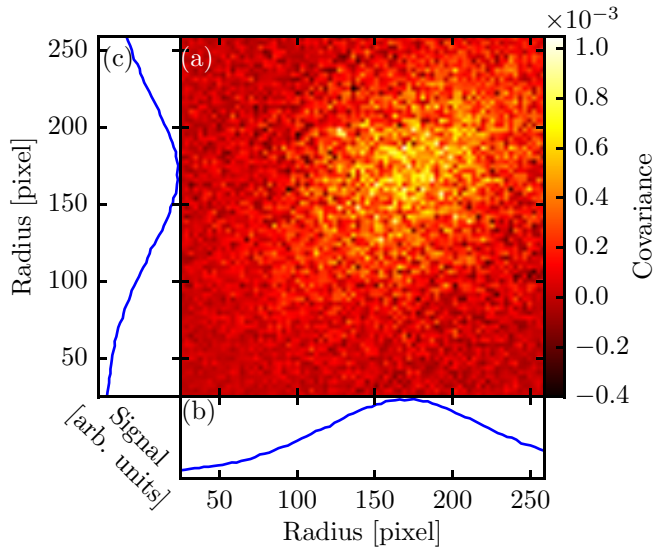


FIG. 16. (a) Radial covariance map of I^+ ions on the top part of the detector with I^+ ions on the bottom half recorded from molecules inside helium droplets. (b),(c) Average radial distribution from the 2D ion image.

isolated molecules and molecules inside He droplets. The difference in speed is ascribed to the iodine colliding with helium atoms on the way out of the droplet or the solvation of the molecule inside the droplet increasing the masses of involved fragments in the Coulomb explosion sharing the same repulsion energy as in the isolated case [45].

C. Covariance analysis of the radial and angular distributions of the I^+ ions

The covariance analysis presented here is based on the image of I^+ ions recorded at the high intensity (3.8×10^{14} W/cm²). The I^+ ion image in Fig. 13(a2) consists of 6.7×10^5 ion hits recorded in 5×10^6 laser shots. First the radial covariance was investigated in the same manner as for the isolated molecules. The covariance map was calculated between I^+ ions hitting the bottom half of the detector with those hitting the top half, and it is shown in Fig. 16(a). The average radial distribution is shown below and to the left of the map in Figs. 16(b) and 16(c). The radial scale is not directly comparable to the one for the isolated molecules due to the extended flight distance used for the droplet measurements. There is, however, a clear correlation between the I^+ ions hitting the bottom half of the detector and those hitting the top half. The correlation is strongest for the I^+ ions detected between 120 pixels and 220 pixels. The covariance map for molecules inside helium droplets is less confined to the A diagonal compared to the isolated molecules. This fits with the interpretation that some of the I^+ ions are being slowed down on the way out of the droplet, leading to a broader distribution of velocities. Also a distribution of fragmenting (exploding) species of the molecule inside the droplet, i.e., different solvation complexes, possibly with different symmetries, would broaden the distribution of velocities. Thus, correlations can occur at a broader range of velocities.

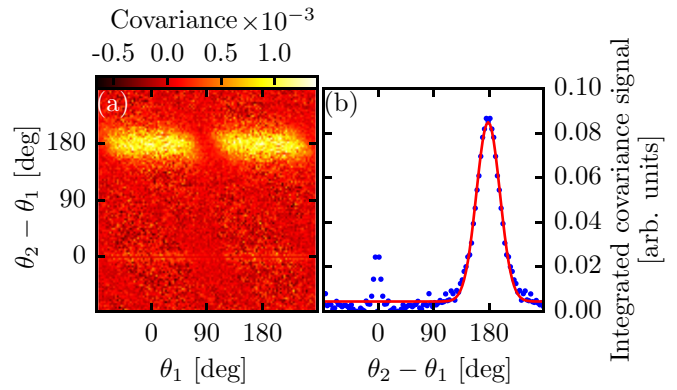


FIG. 17. (a) Angular covariance map for I^+ ions from molecules inside helium droplets as a function of emission angle θ_1 and difference angle $\theta_2 - \theta_1$. (b) Integrated covariance as a function of the difference angle $\theta_2 - \theta_1$.

Next the angular covariance map is calculated for I^+ ions detected between 70 pixels and 260 pixels to investigate the validity of the axial recoil approximation. The angular covariance map shows the same features as for the isolated molecules, and only the rotated angular covariance map is displayed in Fig. 17. Similar to the isolated molecule case, two distinct oblong islands, centered around $\theta_1 = 0^\circ$ and $\theta_1 = 180^\circ$ with the difference angle $\theta_2 - \theta_1 = 180^\circ$, are present. As for the isolated molecules, the covariance map is integrated along θ_1 and the resulting distribution is shown in Fig. 17(b).

Unlike the case for the isolated molecules (Fig. 8), no broad, weak distribution centered around 0° is observed in the integrated covariance distribution. Thus, there are essentially no false covariances. We do not have an obvious explanation for this, but it appears that the fluctuations in the I^+ ion count rate from molecules inside helium droplets is less than those for the isolated molecules under the experimental conditions applied. The narrow spike at 0° is an artefact of the detection and does not influence the correlation analysis. The FWHM of the integrated covariance signal at 180° was determined to be $45 \pm 1^\circ$. By comparison, the FWHM for the outer channel of the isolated molecules is 28° and $30 \pm 0.3^\circ$ when averaged over both the inner and outer channel. This shows that the deviation from axial recoil is significantly larger for molecules inside He droplets compared to isolated molecules.

V. DISCUSSION AND CONCLUSION

The main finding of the current work is the quantitative measure for the degree of axial recoil in the Coulomb explosion process of DIB molecules producing a pair of oppositely traveling I^+ ions. Recording the distribution of the relative angular emission of the two I^+ ions as in Figs. 8 and 17 should make it possible to correct future measurements of the spatial orientation of DIB molecules for the deviation from axial recoil in the Coulomb explosion process. In the many current applications of aligned or oriented molecules, an improvement in the accuracy of how molecules are turned in space will be useful.

The covariance analysis showed that the width of the relative angular distribution of the two I^+ ions is 30° for isolated molecules and 45° for molecules in He droplets. Our

experiment does not provide insight into the mechanisms that cause the deviation from axial recoil, but we speculate that both charge asymmetries in the Coulomb explosion process (for instance, if an electron is removed from a H atom on one side of the benzene ring but not from any H atoms on the other side) and distortion of the molecular geometry during the Coulomb explosion process due to vibrations [47,48] play a role. For the molecules inside He droplets, additional factors can contribute to blurring the axial recoil. First, as the I^+ fragment ions travel out of the droplet, they will interact with the He atoms. Previous studies of photodissociation showed that this interaction can be modeled as binary collisions [45], which will tend to blur the initial recoil direction. Second, at the intensities of the probe pulse, not only the molecules but also some of the He atoms in the immediate vicinity of the molecules are ionized. It is likely that this ionization not always occur symmetric with respect to the molecular structure, which could lead to a deviation in the emission of the I^+ ions from the I-I axis during the Coulomb explosion.

To illustrate the implication of the deviation from axial recoil characterized in the present work, we simulated the ion emission directions that replicate the covariance maps measured here. The simulation reveals that the degree of alignment which would be measured for a perfectly aligned molecular ensemble is $\langle \cos^2 \theta_{2D} \rangle = 0.979$ for isolated DIB molecules and $\langle \cos^2 \theta_{2D} \rangle = 0.947$ for DIB molecules inside He droplets. Had the axial recoil been perfect, $\langle \cos^2 \theta_{2D} \rangle$ would be equal to 1. Ideally, the effect of nonaxial recoil should be deconvoluted from the measured angular distributions of the ions following Coulomb explosion such that the true degree of alignment can be determined. This is particularly important if the degree of alignment is very high. Currently, we are exploring how this deconvolution can be implemented based on covariance measurements, similar to those presented here, and comparison to simulated results. Details will be presented in Ref. [49].

The lack of axial recoil is expected to occur for many other polyatomic molecules. As an example, we applied the

current analysis to 1,4-dibromobenzene (DBrB). In this case, Br^+ ions were recorded and the subsequent analysis occurred similar to that of DIB. The width of the integrated angular covariance distribution was measured to $32 \pm 0.4^\circ$ for the isolated molecules and $51 \pm 0.7^\circ$ for molecules in helium droplets. As for DIB, the measurements show that the deviation from axial recoil is significantly higher for molecules inside He droplets compared to isolated molecules. We note that the deviation from axial recoil of the DBrB molecules inside He droplets seems somewhat larger than for DIB molecules in He droplets. A plausible explanation is that the lower mass of the Br^+ ions makes them more susceptible to changes of their initial recoil direction, from the Coulomb explosion, due to collisions with the He atoms on the way out of the droplet than the heavier I^+ ions.

The DIB and DBrB molecules were chosen because they contain two identical atoms. The relative emission of two iodine or bromine ions recoiling from each end of the molecules could be characterized by covariance analysis of the ion angular distributions recorded with a velocity map imaging spectrometer and a standard CCD camera. This approach should be directly applicable to several other molecules, such as CS_2 , CO_2 , and C_2H_2 , but it can be extended to a much larger class of molecules if different ion species from the Coulomb explosion can be recorded individually for each laser shot. This is possible, for instance, by employing a PIMMS camera [42]. Such comprehensive data should also allow an exploration of the accuracy of Coulomb explosion to probe the orientation of more than one molecular axis, which is needed for characterizing three-dimensional alignment [21,50–52].

ACKNOWLEDGMENTS

Support from European Research Council-AdG (Project No. 320459, DropletControl), Villum Fonden, Lundbeckfonden, Carlsbergfondet, and Natur og Univers, Det Frie Forskningsråd is greatly acknowledged.

-
- [1] Z. Vager, R. Naaman, and E. P. Kanter, *Science* **244**, 426 (1989).
 - [2] J. H. Posthumus, *Rep. Prog. Phys.* **67**, 623 (2004).
 - [3] Y. Muramatsu, K. Ueda, N. Saito, H. Chiba, M. Lavollée, A. Czasch, T. Weber, O. Jagutzki, H. Schmidt-Böcking, R. Moshhammer, U. Becker, K. Kubozuka, and I. Koyano, *Phys. Rev. Lett.* **88**, 133002 (2002).
 - [4] H. Iwayama, K. Nagaya, H. Murakami, Y. Ohmasa, and M. Yao, *J. Phys. B: Atom. Mol. Opt. Phys.* **43**, 185207 (2010).
 - [5] O. Kornilov, M. Eckstein, M. Rosenblatt, C. P. Schulz, K. Motomura, A. Rouzée, J. Klei, L. Foucar, M. Siano, A. Lübcke, F. Schapper, P. Johnsson, D. M. P. Holland, T. Schlathölder, T. Marchenko, S. Düsterer, K. Ueda, M. J. J. Vrakking, and L. J. Frasinski, *J. Phys. B: Atom. Mol. Opt. Phys.* **46**, 164028 (2013).
 - [6] B. Erk, D. Rolles, L. Foucar, B. Rudek, S. W. Epp, M. Cryle, C. Bostedt, S. Schorb, J. Bozek, A. Rouzée, A. Hundertmark, T. Marchenko, M. Simon, F. Filsinger, L. Christensen, S. De, S. Trippel, J. Küpper, H. Stapelfeldt, S. Wada, K. Ueda, M. Swiggers, M. Messerschmidt, C. D. Schröter, R. Moshhammer, I. Schlichting, J. Ullrich, and A. Rudenko, *Phys. Rev. Lett.* **110**, 053003 (2013).
 - [7] B. Erk, R. Boll, S. Trippel, D. Anielski, L. Foucar, B. Rudek, S. W. Epp, R. Coffee, S. Carron, S. Schorb, K. R. Ferguson, M. Swiggers, J. D. Bozek, M. Simon, T. Marchenko, J. Küpper, I. Schlichting, J. Ullrich, C. Bostedt, D. Rolles, and A. Rudenko, *Science* **345**, 288 (2014).
 - [8] M. Pitzer, M. Kunitski, A. S. Johnson, T. Jahnke, H. Sann, F. Sturm, L. P. H. Schmidt, H. Schmidt-Böcking, R. Dörner, J. Stohner, J. Kiedrowski, M. Reggelin, S. Marquardt, A. Schießer, R. Berger, and M. S. Schöffler, *Science* **341**, 1096 (2013).
 - [9] H. Stapelfeldt, E. Constant, and P. B. Corkum, *Phys. Rev. Lett.* **74**, 3780 (1995).
 - [10] Y. H. Jiang, A. Rudenko, O. Herrwerth, L. Foucar, M. Kurka, K. U. Kühnel, M. Lezius, M. F. Kling, J. van Tilborg, A. Belkacem, K. Ueda, S. Düsterer, R. Treusch, C. D. Schröter, R. Moshhammer, and J. Ullrich, *Phys. Rev. Lett.* **105**, 263002 (2010).
 - [11] H. Ibrahim, B. Wales, S. Beaulieu, B. E. Schmidt, N. Thiré, E. P. Fowe, É. Bisson, C. T. Hebeisen, V. Wanie, M. Giguère, J.-C. Kieffer, M. Spanner, A. D. Bandrauk, J. Sanderson, M. S. Schuurman, and F. Légaré, *Nat. Commun.* **5**, 4422 (2014).

- [12] L. Christensen, J. H. Nielsen, C. B. Brandt, C. B. Madsen, L. B. Madsen, C. S. Slater, A. Lauer, M. Brouard, M. P. Johansson, B. Shepperson, and H. Stapelfeldt, *Phys. Rev. Lett.* **113**, 073005 (2014).
- [13] H. Stapelfeldt and T. Seideman, *Rev. Mod. Phys.* **75**, 543 (2003).
- [14] P. W. Dooley, I. V. Litvinyuk, K. F. Lee, D. M. Rayner, M. Spanner, D. M. Villeneuve, and P. B. Corkum, *Phys. Rev. A* **68**, 023406 (2003).
- [15] O. Ghafur, A. Rouzee, A. Gijbetsen, W. K. Siu, S. Stolte, and M. J. J. Vrakking, *Nat. Phys.* **5**, 289 (2009).
- [16] L. Holmegaard, J. H. Nielsen, I. Nevo, H. Stapelfeldt, F. Filsinger, J. Küpper, and G. Meijer, *Phys. Rev. Lett.* **102**, 023001 (2009).
- [17] G. H. Dunn and L. J. Kieffer, *Phys. Rev.* **132**, 2109 (1963).
- [18] R. N. Zare, *J. Chem. Phys.* **47**, 204 (1967).
- [19] R. Zare and D. Herschbach, *Proc. IEEE* **51**, 173 (1963).
- [20] A. Korobenko, A. A. Milner, and V. Milner, *Phys. Rev. Lett.* **112**, 113004 (2014).
- [21] X. Ren, V. Makhija, and V. Kumarappan, *Phys. Rev. Lett.* **112**, 173602 (2014).
- [22] T. Kierspel, J. Wiese, T. Mullins, J. Robinson, A. Aquila, A. Barty, Richard Bean, R. Boll, S. Boutet, P. Bucksbaum, H. N. Chapman, L. Christensen, A. Fry, Mark Hunter, J. E. Koglin, M. Liang, V. Mariani, A. Morgan, A. Natan, Vladimir Petrovic, D. Rolles, A. Rudenko, K. Schnorr, H. Stapelfeldt, S. Stern, Jan Thøgersen, C. H. Yoon, F. Wang, S. Trippel, and J. Küpper, *J. Phys. B: Atom. Mol. Opt. Phys.* **48**, 204002 (2015).
- [23] D. Pentlehner, J. H. Nielsen, A. Slenczka, K. Mølmer, and H. Stapelfeldt, *Phys. Rev. Lett.* **110**, 093002 (2013).
- [24] D. Pentlehner, J. H. Nielsen, L. Christiansen, A. Slenczka, and H. Stapelfeldt, *Phys. Rev. A* **87**, 063401 (2013).
- [25] L. Christiansen, J. H. Nielsen, D. Pentlehner, J. G. Underwood, and H. Stapelfeldt, *Phys. Rev. A* **92**, 053415 (2015).
- [26] U. Even, J. Jortner, D. Noy, N. Lavie, and C. Cossart-Magos, *J. Chem. Phys.* **112**, 8068 (2000).
- [27] A. T. J. B. Eppink and D. H. Parker, *Rev. Sci. Instrum.* **68**, 3477 (1997).
- [28] J. P. Toennies and A. F. Vilesov, *Ang. Chem. Intl. Ed.* **43**, 2622 (2004).
- [29] T. Zuo and A. D. Bandrauk, *Phys. Rev. A* **52**, R2511 (1995).
- [30] T. Seideman, M. Y. Ivanov, and P. B. Corkum, *Phys. Rev. Lett.* **75**, 2819 (1995).
- [31] E. Constant, H. Stapelfeldt, and P. B. Corkum, *Phys. Rev. Lett.* **76**, 4140 (1996).
- [32] H. Sakai, H. Stapelfeldt, E. Constant, M. Y. Ivanov, D. R. Matusek, J. S. Wright, and P. B. Corkum, *Phys. Rev. Lett.* **81**, 2217 (1998).
- [33] L. J. Frasinski, K. Codling, and P. A. Hatherly, *Science* **246**, 1029 (1989).
- [34] W. A. Bryan, W. R. Newell, J. H. Sanderson, and A. J. Langley, *Phys. Rev. A* **74**, 053409 (2006).
- [35] J. Mikosch and S. Patchkovskii, *J. Mod. Opt.* **60**, 1439 (2013).
- [36] J. Mikosch and S. Patchkovskii, *J. Mod. Opt.* **60**, 1426 (2013).
- [37] G. A. Garcia, L. Nahon, and I. Powis, *Rev. Sci. Instrum.* **75**, 4989 (2004).
- [38] M. Alagia, P. Candori, S. Falcinelli, M. Lavollée, F. Pirani, R. Richter, S. Stranges, and F. Vecchiocattivi, *J. Phys. Chem. A* **113**, 14755 (2009).
- [39] L. Holmegaard, Ph.D. thesis, Aarhus University, 2006.
- [40] S. B. Hendricks, L. R. Maxwell, V. L. Mosley, and M. E. Jefferson, *J. Chem. Phys.* **1**, 549 (1933).
- [41] J. L. Hansen, J. H. Nielsen, C. B. Madsen, A. T. Lindhardt, M. P. Johansson, T. Skrydstrup, L. B. Madsen, and H. Stapelfeldt, *J. Chem. Phys.* **136**, 204310 (2012).
- [42] C. S. Slater, S. Blake, M. Brouard, A. Lauer, C. Vallance, J. J. John, R. Turchetta, A. Nomerotski, L. Christensen, J. H. Nielsen, M. P. Johansson, and H. Stapelfeldt, *Phys. Rev. A* **89**, 011401 (2014).
- [43] A. Nomerotski, M. Brouard, E. Campbell, A. Clark, J. Crooks, J. Fopma, J. J. John, A. J. Johnsen, C. Slater, R. Turchetta, C. Vallance, E. Wilman, and W. H. Yuen, *J. Instrum.* **5**, C07007 (2010).
- [44] C. Vallance, M. Brouard, A. Lauer, C. S. Slater, E. Halford, B. Winter, S. J. King, J. W. L. Lee, D. E. Pooley, I. Sedgwick, R. Turchetta, A. Nomerotski, J. J. John, and L. Hill, *Phys. Chem. Chem. Phys.* **16**, 383 (2014).
- [45] A. Braun and M. Drabbels, *J. Chem. Phys.* **127**, 114304 (2007).
- [46] A. Braun and M. Drabbels, *Phys. Rev. Lett.* **93**, 253401 (2004).
- [47] P. Graham, K. W. D. Ledingham, R. P. Singhal, T. McCanny, S. M. Hankin, X. Fang, D. J. Smith, C. Kosmidis, P. Tzallas, A. J. Langley, and P. F. Taday, *J. Phys. B: Atom. Mol. Opt. Phys.* **32**, 5557 (1999).
- [48] M. Comstock, V. Senekerimyan, and M. Dantus, *J. Phys. Chem. A* **107**, 8271 (2003).
- [49] L. Christiansen, B. Shepperson, D. Pentlehner, H. Stapelfeldt, and L. Christensen (unpublished).
- [50] J. J. Larsen, K. Hald, N. Bjerre, H. Stapelfeldt, and T. Seideman, *Phys. Rev. Lett.* **85**, 2470 (2000).
- [51] I. Nevo, L. Holmegaard, J. H. Nielsen, J. L. Hansen, H. Stapelfeldt, F. Filsinger, G. Meijer, and J. Küpper, *Phys. Chem. Chem. Phys.* **11**, 9912 (2009).
- [52] V. Makhija, X. Ren, and V. Kumarappan, *Phys. Rev. A* **85**, 033425 (2012).